Peer-reviewed version available at Remote Sens. 2019, 11, 295; doi:10.3390/rs11030295

Article

Assessing Diurnal Variability of Biogeochemical Processes using the Geostationary Ocean Color Imager (GOCI)

Javier Concha [1,2,*], Antonio Mannino [1], Bryan Franz [1] and Wonkook Kim [3]

[1] Ocean Ecology Lab, NASA Goddard Space Flight Center, Greenbelt, MD, USA
[2] Universities Space Research Association, Columbia, MD, USA
[3] Korea Institute of Ocean Science and Technology, Busan, Republic of Korea
* Correspondence: javier.concha@nasa.gov; Tel.: +1-301-286-1069

Version November 2, 2018 submitted to Preprints

Abstract: Short-term (hours) biological and biogeochemical processes cannot be fully captured by the current suite of polar-orbiting satellite ocean color sensors, as their temporal resolution is limited to potentially one clear image per day. Geostationary sensors, such as the Geostationary Ocean Color Imager (GOCI) from the Republic of Korea, allow the study of these short-term processes because their geostationary orbits permit the collection of multiple images throughout each day. To assess the capability to detect changes in water properties caused by these processes, however, requires an understaning of the uncertainties introduced by the instrument and/or geophysical retrieval algorithms. This work presents a study of the variability during the day over a water region of low-productivity with the assumption that only small changes in the water properties occur during the day over the area of study. The complete GOCI mission data were processed using the SeaDAS/l2gen package. Filtering criteria were applied to assure the quality of the data. Relative differences with respect to the midday value were calculated for each hourly observation of the day. Also, the influence of the solar zenith angle in the retrieval of remote sensing reflectances and derived products was analyzed. We determined that the uncertainties in water-leaving "remote-sensing" reflectance (R_{rs}) for the 412, 443, 490, 555, 660 and 680 nm bands on GOCI are 8.05×10^{-4}, 5.49×10^{-4}, 4.48×10^{-4}, 2.51×10^{-4}, 8.83×10^{-5}, and 1.36×10^{-4} sr^{-1}, respectively, and 1.09×10^{-2} mg m^{-3} for the chlorophyll-a concentration (Chl-*a*), 2.09×10^{-3} m^{-1} for the absorption coefficient of chromophoric dissolved organic matter at 412 nm ($a_g(412)$), and 3.7 mg m^{-3} for particulate organic carbon (POC). We consider these to be the floor values for detectable changes in the water properties due to biological, physical or chemical processes.

Keywords: Geostationary Ocean Color Imager (GOCI); Ocean Color; Diurnal Dynamics; Diurnal Variability; Uncertainties

1. Introduction

Ocean waters are highly dynamic due to environmental factors such as heating of the surface ocean layer, fluctuation in wind intensity, surface currents, tidal cycles, changes in vertical mixing layers, and variation of sunlight radiation. These dynamics can vary on timescales from $<$ 1 hour to a few weeks, and current low earth orbit (LEO) assets (e.g. Moderate Resolution Imaging Spectroradiometer (MODIS) [1], Visible Infrared Imaging Radiometer Suite (VIIRS) [2]) do not have the temporal resolution needed to capture these short term dynamics. These sub-diurnal and multi-day (short term) changes affect different marine ecosystem processes and constituent concentrations: ocean primary production, carbon stocks, export production, and phytoplankton community composition, among others. Climate models and forecasting abilities could benefit from constraining the magnitude and the uncertainty in these variables.

Ocean color sensors in geostationary orbit (GEO) can help to constrain these uncertainties because of their sub-diurnal acquisition capability. Republic of Korea's Geostationary Ocean Color Imager

(GOCI), launched in 2010, is the first and only (to date) operational geostationary ocean color sensor [3], and it has proven to be capable of detecting sub-diurnal dynamics. Ryu et al. (2011) [4] utilized GOCI data to study the temporal variation of coastal waters in Korea. A variety of algorithms have been developed that utilize GOCI spectral observations to retrieve water-column constituents, including concentrations of the phytoplankton pigment chlorophyll-a (Chl-*a*) and total suspended material (TSM) [5,6]. GOCI data have also been used to determine the diurnal submesoscale variability of turbidity fronts [7], internal waves [8], and red ties and green algae [9,10]. The success of GOCI has prompted the development of future GEO missions such as GOCI-II, scheduled to be launched in 2019, and formulation studies on a European geostationary satellite GEO-OCAPI. NASA has conducted and recently concluded pre-formulation studies for the Geostationary Coastal and Air Pollution Events (GEO-CAPE) mission. Taken together, GEO missions such as these three have the capability to provide quasi-global coverage at low and mid-latitudes [11].

In order to determine whether sub-diurnal and day-to-day differences in GOCI-derived optical and biogeochemical ocean properties are related to real physical, ecological, and biogeochemical processes, the levels of uncertainties of GOCI data products must first be assessed. Hence, the primary objective of this study is to quantify the inherent uncertainties of GOCI remote sensing reflectances (R_{rs}) and derived products when assessing diurnal variability. First, we processed GOCI data to R_{rs} over a clear water region, which is assumed to express little to no diurnal and day-to-day variability due to biology or physical processes. To determine the validity of this assumption, the absence of variability from sub-diurnal to multiple day timescales is investigated. We verified that this assumption holds true at these timescales for our study region. Next, we estimated GOCI R_{rs} and derived biogeochemical product uncertainties within the region of study using two different approaches: 1) an analysis of daily statistics, specifically the daily standard deviation and the percentage coefficient of variation (CV), to estimate the deviation from the daily mean of the overall mission, and 2) the relative difference with respect to a midday value ($R\Delta_t[\%]$) to estimate the deviation from a midday value by time of the day. Also, the effect of the solar zenith angle (SZA) in the retrieval was investigated. Our findings suggest that diurnal variability is discernible with GOCI within a certain level of uncertainties and that there does not appear to be a considerably negative impact from the sensor-solar geometry in the algorithms.

2. Data and Sensor Characteristics

This study focused on ocean color data from GOCI over a specific open ocean region within its coverage area. GOCI's specifications and a description of the study area are described in this section.

2.1. GOCI Data

GOCI, which was launched on 26 June 2010, monitors the Northeast Asian waters surrounding the Korean peninsula, generating eight images per day (from 00:15 Greenwich Mean Time (GMT) to 07:45 GMT at one hour interval or from 9:15 to 16:45 hrs. local time) with a spatial resolution of 500 m at 130^{o}E and 36^{o}N. It covers an area of about 2500 km$\times$2500 km. It has eight spectral bands (6 bands in the visible: 412, 443, 490, 555, 660 and 680 nm; 2 bands in the near infrared (NIR): 745 and 865 nm). GOCI operates in a 2D staring-frame capture mode in a geostationary orbit onboard the Communication Ocean and Meteorological Satellite (COMS) of the Republic of Korea. The data acquisition over the observational coverage area of GOCI is accomplished with a step-and-stare method that takes 16 step-by-step slots by the scan of a poiting mirror with a dedicated CMOS detector array (1432 $\times$ 1415 pixels) [12].

The images used in this analysis span from the beginning of GOCI's mission (May 2011) until January 2018, resulting in a total of about 20,000 images. The GOCI Level-1B calibrated top-of-atmosphere (TOA) radiance data were obtained from the Ocean Biology Distributed Active Archive Center (OB.DAAC) at the NASA's Goddard Space Flight Center, maintained by the Ocean Biology Processing Group (OBPG). The OB.DAAC acts as a mirror site for the GOCI data provided by

the Korea Ocean Satellite Center of the Korea Institute of Ocean Science and Technology. These data are freely available for direct download from the OB.DAAC.

2.2. Area of Study

The area of study (Figure 1 blue box) is an area that covers an open-ocean region of oligotrophic waters located to the south of Japan, with the boundaries north= 28.4950^o, south= 26.0960^o, west=37.3380^o, and east=42.0920^o, centered at $27.33^o N$ and $139.71^o E$. Figure 1 shows the GOCI coverage area (red box) for reference. This area of study will be called GCWS (GOCI Clear Water Subset) region hereafter. This area is the same area used by [13] for obtaining the vicarious calibration gains. The GCWS region is approximately 433×968 GOCI pixels, equivalent to approximately 100,000 km^2. The reasoning behind the selection of this area of study is the assumption that most of the variability in this region during the day will be caused by physical (e.g. solar heating, wind, waves) changes and not by biogeochemical processes (e.g. CO2 fixation). In this manner, the variability in the GOCI-derived products due to water composition will be minimized, and therefore, the variability introduced by sensor radiometric uncertainty (e.g., noise, systematic error), viewing geometry, and algorithm can be analyzed. For this region, the range of SZA during the acquisition time varies between 0^o and 90^o through the year, and from approximately 29^o to 37^o for the sensor (viewing) zenith angle. The boundaries of the GCWS region were selected inside the slot located in the lower right corner of the L1B image (slot number 13 in [14]) to avoid the Stray-Light-Driven Interslot Radiometric Discrepancy (ISRD) at the near-boundary of the interslot areas [14,15]. It has been estimated that the stray-light-driven radiometric anomalies could reach up to 20% in some bands, and therefore, the potentially affected areas were excluded in this study.

The area of study is located south of Japan (Figure 1), in the northwestern fringe of the North Pacific Subtropical Gyre (NPSG) in a transition region between its western boundary current, i.e. the Kuroshio Current, and the subtropical countercurrent (STCC) [16]. The NPSG gyre expands or contracts depending on the season following the seasonal strength of the winds and convective upper-ocean mixing [17,18], which may lead to seasonal changes in the optical properties of the area of study from oligotrophic and mesotrophic conditions. Furthermore, because the study region is at the limit of NPSG, it may be affected by different types of physical forcing than the ones affecting the gyres. For instance, fronts or winds may induce upwelling, providing nutrients to the euphotic zone. Combined with the fact that the nutricline is much shallower in the fringes of the gyre than in its interior, this can contribute to a larger phytoplankton growth compared with the gyres. The Chl-*a* concentration in the study region ranges from 0.05 mg m^{-3} to 0.2 mg m^{-3} (as described in section 4.1), depending on the season, a range comparable to the one reported by [18] with a mean satellite-derived Chl-*a* concentration in the NPSG gyre ranging between 0.07 mg m^{-3} and 0.11 mg m^{-3}.

3. Processing Approach

The analysis of the uncertainties is made over the GOCI-derived Level-2 (L2) products that include remote-sensing reflectance, chlorophyll-*a* concentration (Chl-*a*), chromophoric dissolved organic matter (CDOM) absorption at 412 nm ($a_g(412)$) and particulate organic carbon (POC). After processing the data to L2, these data were screened for quality assurance.

3.1. Conversion to Level 2

GOCI geolocated and radiometricly calibrated (Level-1B) data (L1B) were processed to Level-2 biogeophysical products (L2) using the multisensor Level-1 to Level-2 generator (l2gen) version 9.2.0-V2017.0.3 distributed with the SeaWiFS Data Analysis System (SeaDAS) (http://seadas.gsfc.nasa.gov/). The l2gen code reads Level-1B observed top-of-atmosphere (TOA) radiances, applies one of the atmospheric correction scheme available, and outputs various products such as radiances or reflectances (e.g. spectral remote-sensing reflectance, $R_{rs}(\lambda)$) and derived geophysical parameter (e.g.

Preprints (www.preprints.org) | NOT PEER-REVIEWED | Posted: 2 November 2018 doi:10.20944/preprints201811.0042.v1

Peer-reviewed version available at Remote Sens. 2019, 11, 295; doi:10.3390/rs11030295

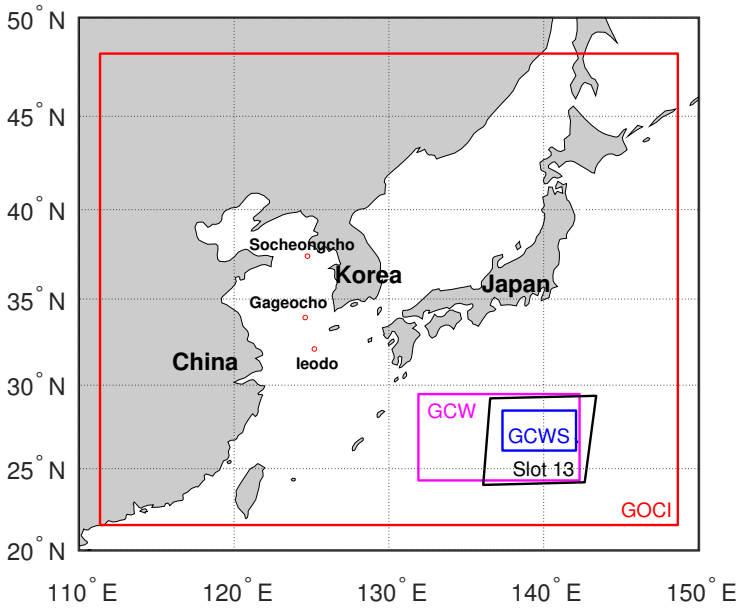

Figure 1. The study area (GCWS region; blue box) is located over oligotrophic waters to the south of Japan within the coverage area of GOCI (red box). This area was selected because of the assumption that the most of the daily variability is caused by physical factors. The GCWS region covers 433 × 968 pixels, which is equivalent to 100,000 km^2. Figure taken from Concha et al. (2018) [13].

chlorophyll-*a* concentration). As part of the l2gen processing, each pixel is masked with different flags that reflect warnings or errors generated during the processing to assure the quality of the data [19].

The atmospheric correction scheme applied to this study was the default algorithm for GOCI (aer_opt=-2) that uses an estimation of the aerosol contribution described by Gordon & Wang (1994) [20], including a near infrared (NIR) iterative correction by Bailey et al. (2010) [21] and a suite of aerosol models developed by Ahmad et al (2010) [22] with selection that is dependent on relative humidity and the spectral slope observed in two NIR channels. GOCI's two near infrared (NIR) bands at 745 and 865 nm were used for the aerosol model selection. This atmospheric correction approach assumes a plane-parallel geometry, ignoring earth curvature, for the vector radiative transfer simulations used for the computation of the look-up tables of Rayleigh and aerosol reflectance. A vicarious calibration specific for GOCI was applied, based on match-ups with MODIS-Aqua over the same GCWS region [13].

3.2. Data screening

For the analysis of uncertainties described in the next sections, we chose to use a single value that represents each L2 product: the filtered mean. To ensure a good quality of the data used for the analysis, an exclusion criterion (filtering) that is based on [19] was applied for the calculation of this filtered mean (Figure 2), and it is described as follows. In order to avoid the effect of outliers in the calculations, the following screening criteria were applied for selecting the pixels within the GCWS region to be used for the calculation of the filtered mean:

$$(Med - 1.5 * \sigma) < X_i < (Med + 1.5 * \sigma) \quad (1)$$

where X_i is the i^{th} filtered pixel within the GCWS region, Med is the median value of the unflagged pixels, and σ is the standard deviation of the unflagged pixels. Then, the filtered mean was calculated:

$$\text{Filtered Mean} = \frac{\sum_{i}^{NFP} X_i}{NFP} \quad (2)$$

Preprints (www.preprints.org) | NOT PEER-REVIEWED | Posted: 2 November 2018 doi:10.20944/preprints201811.0042.v1

Peer-reviewed version available at Remote Sens. 2019, 11, 295; doi:10.3390/rs11030295

where NFP is the Number Filtered Pixels, i.e. the number of unflagged values within $Med \pm 1.5 * \sigma$. Note the difference with Equation 4 in [19], in which the mean of the unfiltered data was used instead of the median, as in this case. The use of the median value for the calculation of the filtered mean minimizes the influence of outliers.

A coefficient of variation (CV), which is defined as the standard deviation divided by the mean, is calculated for the R_{rs} in the blue and green bands and the aerosol optical thickness at 865 nm product derived for each L2 file. Then, the median of all these CV values for each L2 file is recorded ($Med[CV]$). Then, only L2 products with an associated ($Med[CV]$ smaller than 0.25 (25%) were used for the uncertainties analysis. Also, to have statistical confidence in the filtered mean value, NFP is required to be at least a third of the number of total pixels in the GCWS region (i.e. $NFP \geq NTP/3 = 139,714$) for the L2 product to be considered in the analysis. This is equivalent to stating that at least a third of the area of the GCWS region has valid pixel values associated with it. Both of these thresholds, the minimal valid area and the maximum $Med[CV]$, were determined through a trial-and-error method that maximized a tradeoff between sufficiency of data values for statistical robustness and the influence of outliers.

Additionally, we excluded L2 products with solar and sensor zenith of the center pixel that exceeded 75^o and 60^o, respectively, to avoid extreme solar and viewing geometries [19]. However, the sensor zenith angle is between 29^o and 37^o for this study region, and therefore, this criterion did not exclude any pixels.

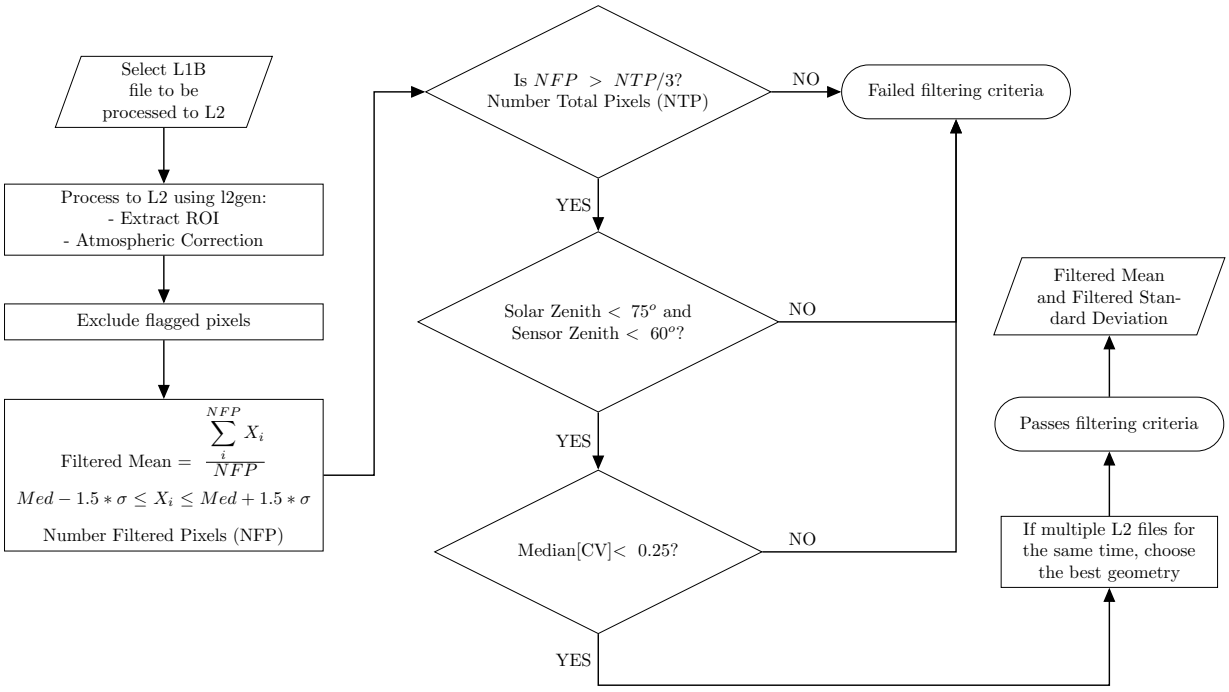

Figure 2. Methodology to calculate the filtered mean and standard deviation for each L2 product including the exclusion criteria applied to ensure good data quality

3.3. Bio-Optical Algorithms

In addition to the R_{rs} products, three more bio-optical algorithms were used to study uncertainties in diurnal variabilities using GOCI. Two of them were the default global algorithms found in SeaDAS/l2gen, and the third one is a CDOM absorption retrieval algorithm currently under testing.

3.3.1. Chlorophyll-*a* Concentration (Chl-*a*)

The standard Chl-*a* product produced by the OBPG blends two algorithms. The maximum band ratio algorithm (OCx) relies on empirically derived relationships that statistically relate *in situ* pigment

concentration with field-measured band ratios of R_{rs}, of blue and green bands [23]. This algorithm is updated regularly to include the most recent field measurements. OBPG recently adopted the color index (CI) Chl-*a* algorithm of Hu et al. (2012) [24], a three-band difference algorithm, to compute Chl-*a* within clear waters. OBPG generates a single Chl-*a* product (as the standard Chl-*a* product) using both OCx and CI algorithms, where CI-derived values are applied when Chl-*a* < 0.15 mg m^{-3} and OCx when Chl-*a* is > 0.2 mg m^{-3}. Weighted Chl-*a* values are computed for the interval between these values to assure a smooth transition for the merged data product. The blended algorithm is commonly referred to as OCI [24].

Briefly, the CI algorithm for GOCI has the following form:

$$CI = R_{rs}(555) - \left[R_{rs}(443) + \frac{(555-443)}{(660-443)} \times [R_{rs}(660) - R_{rs}(443)]\right]$$
$$Chl_{CI} = 10^{0.4909+191.6590\times CI},\ CI \leq -0.0005\ sr^{-1} \quad (3)$$

and the standard OCx algorithm has the form:

$$log_{10}(chlor\_a) = a_0 + \sum_{i=1}^{4} a_i \left[log_{10}\left(\frac{R_{rs}(\lambda_{blue})}{R_{rs}(\lambda_{green})}\right)\right]^i \quad (4)$$

where the coefficients $a_0, ..., a_4$ are sensor specific. For GOCI, the bands used for the OC2 version are 490 and 555 nm and for the OC3 are 443, 490, 555 nm.

where the coefficients $a_0, ..., a_4$ are sensor specific. For GOCI, the 3-band version of OCx (OC3) is used, with the 443, 490, 555 nm bands and the coefficients $a_0 = 0.2515$, $a_1 = -2.3798$, $a_2 = 1.5823$, $a_3 = -0.6372$ and $a_4 = -0.5692$.

3.3.2. Particulate Organic Carbon (POC)

The standard algorithm to retrieve the concentration of particulate organic carbon (POC) is based on an empirical relationship between *in situ* POC and blue-to-green band ratios of R_{rs} [25]. This algorithm uses the 443 and 555 nm bands for GOCI:

$$POC = 203.2 \times \left[\frac{R_{rs}(443)}{R_{rs}(555)}\right]^{-1.034} \quad (5)$$

3.3.3. Chromophoric Dissolved Organic Matter Absorption Coefficient at 412 nm ($a_g(412)$))

Mannino et al. (2014) [26] developed an algorithm for the retrieval of chromophoric dissolved organic matter (CDOM) absorption at 412 nm ($a_g(412)$)) over water along the northeastern U.S. coast. This algorithm was initially implemented for SeaWiFS and MODIS Aqua and now it is included in l2gen as ag_412_mlrc for testing. It is based on field measurements collected throughout the continental margin of the northeastern U.S. from 2004 to 2011. This algorithm involves a least squares linear regression of $a_g(\lambda)$) with multiple R_{rs} bands within a multiple linear regression (MLR) analysis. The bands used in this case are the 443 and 555 nm bands. This algorithm takes the following form:

$$Y = -2.784 - 1.146 \times Ln[R_{rs}(443)] + 1.008 \times Ln[R_{rs}(555)]$$
$$a_g(412) = e^Y \quad (6)$$

4. Results and Discussion

4.1. Time Series

The time series of R_{rs} exhibit an expected seasonality with a recurrent pattern for all years, more evident in the blue bands (Figure 3), due to biological processes occurring in the area of study. This is

corroborated with the Chl-*a*, $a_g(412)$ and POC products (Figure 4). The Chl-*a* seasonal signal suggests a phytoplankton productivity increase during winter and early spring. The peak of the time series in early spring resembles the behavior of the phytoplankton growth occurring in the North Pacific Subtropical Gyre (NPSG) [18].

These time series were created with filtered mean, and for each day there are potentially eight values displayed, which represents the diurnal variability and explains the daily spread of the data in Figure 3 and Figure 4. Figure 4.(g) shows the SZA for reference. The data from the first part of the mission (before 05-15-2011) were collected during the in-orbit test (IOT) period of the mission and were not included in the following set of analyses. The histograms for the blue bands at 412 and 443 nm (Figure 3.(a,b) exhibit a bimodality due to the seasonal variability of the phytoplankton and possibly CDOM. This behavior is reflected in the biogeochemical products (Figure 4.(a-c)). Also, there are more valid data points in the summer-fall period than the winter-spring one as one would expect for this region due to cloud cover, extreme SZA or atmospheric correction failure.

4.2. Temporal Homogeneity

The primary assumption for this work is that the water over the GCWS region remains temporally and spatially homogeneous over short periods of time, i.e. the optical properties of the water do not change considerably during the daytime nor from day-to-day due to biological or biogeochemical processes. Three-day sequences and diurnal statistics were used in order to test this assumption.

First, one three-day sequence is provided as an example, and then, all three-day sequences are used to obtain a quantitative estimation of both the diurnal and the day-to-day variability. Under ideal circumstances, if the water is temporally and spatially homogeneous, we would expect that all the values during the day are the same and then the value for all days in the three-day sequences are the same too, at least within the uncertainty of the satellite sensor calibration and algorithms applied, and assuming the atmospheric correction algorithm is properly compensating for changes in solar and viewing geometry that influence atmospheric radiant path reflectance, surface reflection/refraction effects, and the bidirectional reflectance of the subsurface light field [27].

Out of the 2500 days for the whole GOCI mission, there are only 96 three-day sequences with valid values for the 412, 443, 490 and 555 nm bands and for all times of the days. Note that there is not a single three-day sequence with valid values for all bands and all times of the day. Given the cloudy nature of the region and the Earth in general, the identification of 96 complete three-day diurnal sequences supports the applicability of such observations from geostationary orbit to study ocean processes in more dynamic areas.

As an example, a three-day sequence is shown in Figure 5 (September 1^{st}-3^{rd}, 2015) to present a specific case of the diurnal and day-to-day variability for the $R_{rs}(\lambda)$ and the Chl-*a*, $a_g(412)$, and POC products. The data were grouped by time of the day (color coded). In this particular case, the diurnal variability for all products is greater than the day-to-day variability for the individual local times for most times. For instance, for $R_{rs}(412)$, the difference between the maximum and minimum for September 1^{st}, 2015 is greater than the difference between maximum and minimum among the three days (September 1^{st}-3^{rd}, 2015) for the 9:00 local time, and the same applies for the rest of the times.

In order to have a quantitative estimation of the diurnal and day-to-day homogeneity for all cases, statistics were calculated for all such three-day sequences. We use the percent coefficient of variation ($CV[\%] = 100 \times SD/mean$ with SD the standard deviation) to describe the dispersion of the three values per sequence and per time of day. Therefore, a $CV[\%]$ was calculated for all three-day sequences separated by time of day ($CV[\%]_{3\text{-day}}$; Figure 6). For instance, for the previous example, a mean and SD were calculated from the three 9:00 local times (one for each day), and then the $CV[\%]_{3\text{-day}}$ was recorded. Therefore, we have 96 $CV[\%]_{3\text{-day}}$ values for the 9:00 local time, 96 for the 10:00 local time, and so on. Figure 6 displays the minimum, maximum, mean and SD for all these $CV[\%]_{3\text{-day}}$ values separated by time of day for all products.

Preprints (www.preprints.org) | NOT PEER-REVIEWED | Posted: 2 November 2018 doi:10.20944/preprints201811.0042.v1

Peer-reviewed version available at Remote Sens. 2019, 11, 295; doi:10.3390/rs11030295

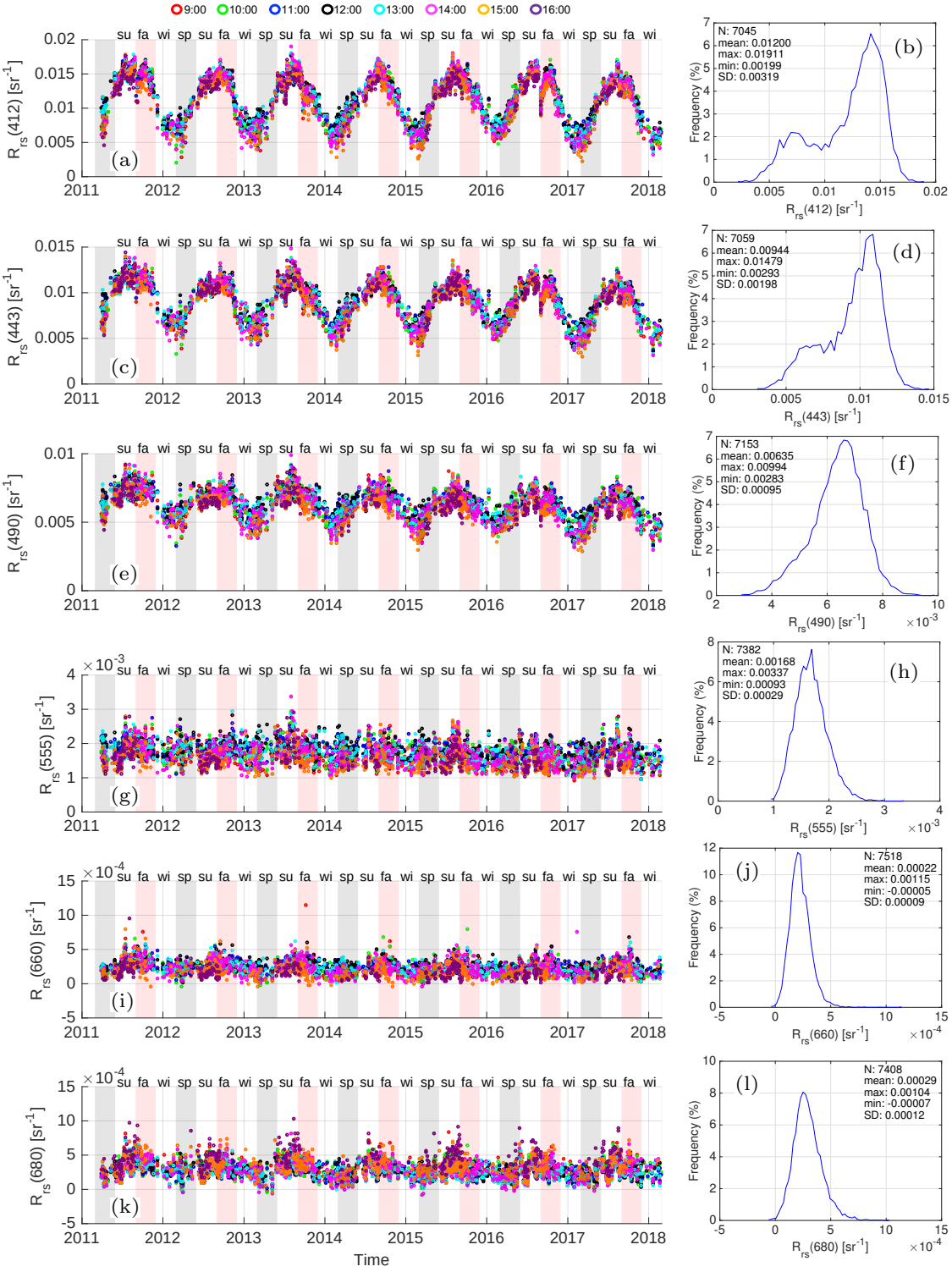

Figure 3. Time Series and histograms for the GCWS region. The complete GOCI mission was processed to Level-2 and a filtered mean was calculated for each image over the GCW region. The data are color coded by time of day in local time. Labels are summer (su), fall (fa), winter (wi) and spring (sp). The histograms show the total number (N), mean, maximum, minimum, and standard deviation (SD) of the values that passed the exclusion criteria.

Preprints (www.preprints.org) | NOT PEER-REVIEWED | Posted: 2 November 2018 doi:10.20944/preprints201811.0042.v1

Peer-reviewed version available at Remote Sens. 2019, 11, 295; doi:10.3390/rs11030295

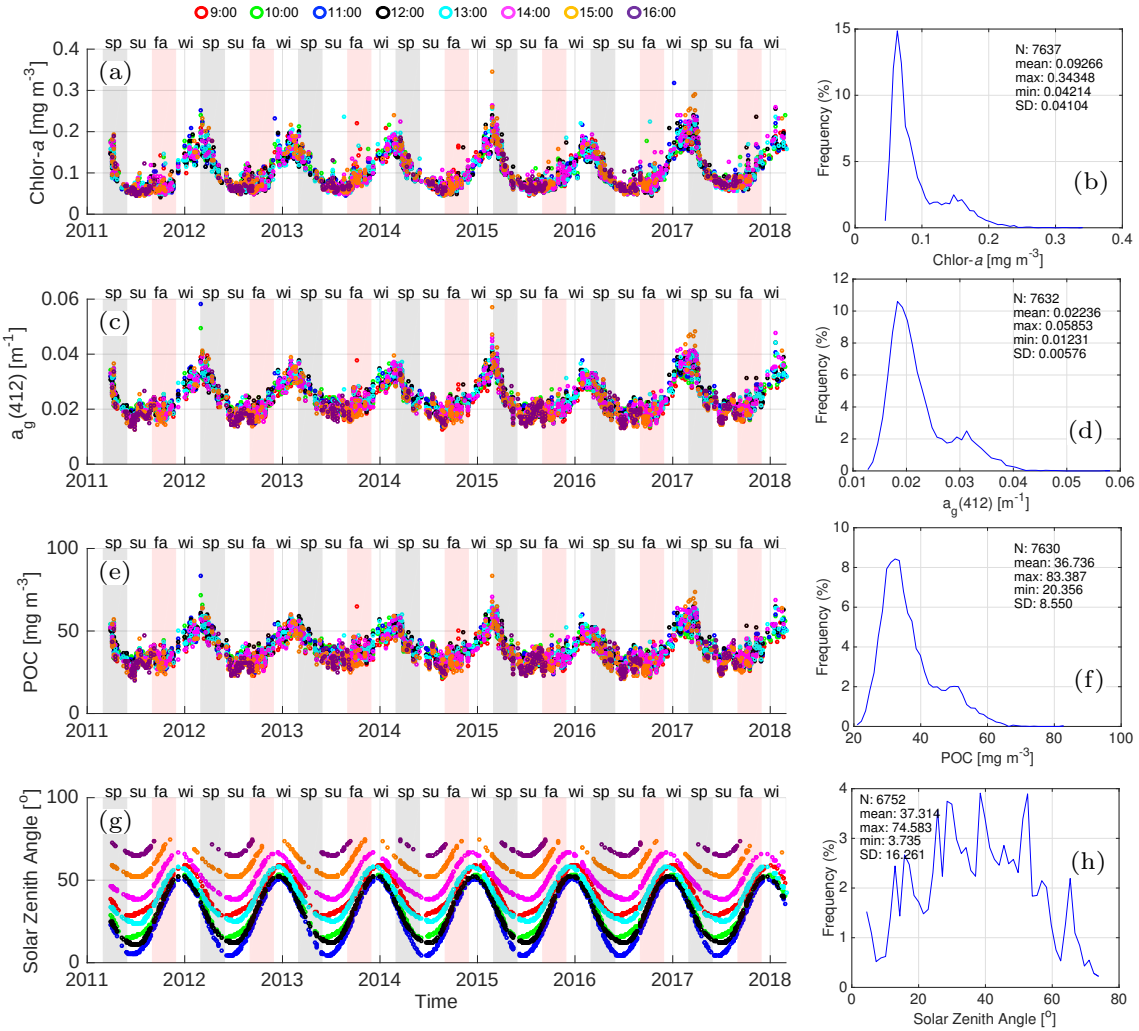

Figure 4. Time Series and histograms for the (a,b) Chlorophyll-*a*, (c,d) $a_g(412)$, (e,f) POC products, and (g) solar zenith angle for the GCWS region. The data are color coded by time of day. The histograms show the total number (N), mean, maximum, minimum, and standard deviation (SD) of the values that passed the exclusion criteria. Labels are summer (su), fall (fa), winter (wi) and spring (sp).

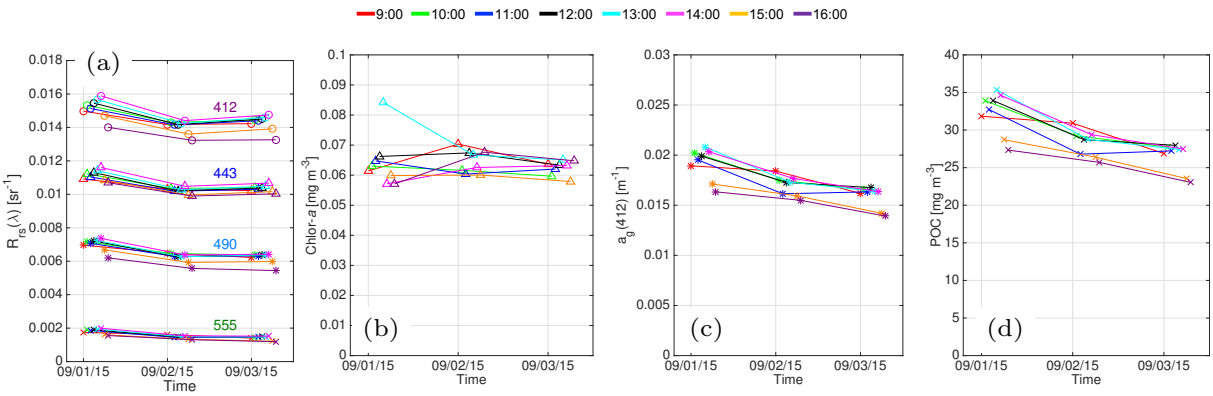

Figure 5. Three-day sequence for (a) $R_{rs}(\lambda)$, (b) Chl-*a*, (c) $a_g(412)$, and (d) POC products. Data are color coded by local time.

We observed that the mean and SD for $CV[\%]_{\text{3-day}}$ remain similar for all times of the day, for all bands and for most products. Also, the mean for $CV[\%]_{\text{3-day}}$ is less than 10% for all times of day for all products, indicating that the day-to-day variability (at least within the confines of the daytime period that GOCI observes) is small. No information is available between the last GOCI observation of the day and first observation on the following day to evaluate variability during that time period. Because the day-to-day (daytime) variability is small, we expect the diurnal variability to be small. If that were not the case, i.e. a significant diurnal variability occurring, then the day-to-day variability should be significant, as well. From the previous analysis, we demonstrated that there is minimal day-to-day and diurnal variability, and therefore, the water over the GCWS region is homogeneous in short periods of time. However, the region of study also exhibits seasonality, as expected, which is reflected in the time series of §4.1.

Next, diurnal statistics were also used to the test homogeneity. A diurnal mean and standard deviation (SD_{diurnal}) were calculated for each day for the whole GOCI mission and used as a statistical metric for diurnal variability. These values were calculated only if three or more values were valid per day. Also, the diurnal percentage coefficient of variation ($CV[\%]_{\text{diurnal}}$) was calculated from these values. Then, the mean of all the diurnal SD values ($\overline{SD}_{\text{diurnal}}$) and the median of the percentage coefficient of variation ($Med[CV[\%]_{\text{diurnal}}]$) were calculated for all the data (all seasons) and for summer alone, when the variability due to change in the water properties are minimal (Table 1). The $\overline{SD}_{\text{diurnal}}$ is an indicator of the temporal stability of the selected homogeneous ocean region throughout the day. We consider that two times the $\overline{SD}_{\text{diurnal}}$ values (i.e. $2 \times \overline{SD}_{\text{diurnal}}$) for summer for the GCWS region provides an approximate measure of the minimum R_{rs} (or derived products) difference required to detect diurnal variability (Table 1). When compared with the RMSE from the R_{rs} matchups between GOCI and AERONET-OC data [13], the $2 \times \overline{SD}_{\text{diurnal}}$ values are up to one order of magnitude smaller for all bands (412-660 nm). The relatively higher AERONET-OC RMSE values can be attributed to in situ measurement uncertainties and the proximity of these sites to land contributing to higher uncertainties in the atmospheric correction from more complex aerosol constituents and absorbing trace gases (ozone and nitrogen dioxide) and more optically complex water types (i.e., higher sediment, biogenic particles, and CDOM) in both time and space. The $Med[CV[\%]_{\text{diurnal}}]$ of R_{rs} for the GCWS region is less than 5% for the blue and green bands, and for the Chl-*a*, $a_g(412)$ and POC products for both all the seasons and only summer. This supports the assumption that the GCWS region is spatially and temporally homogeneous over the course of a day or day-to-day. The significantly higher $Med[CV[\%]_{\text{diurnal}}]$ values for the 660 and 680 nm bands are related to the low ocean reflectance signals at these red wavelengths in the GCWS.

Table 1. The diurnal variability was quantized by calculating the diurnal mean and standard deviation (SD) for each day. The analysis was performed for all the data and for only summer, when there is the smallest variability in the water properties. Two times the mean of diurnal SD ($2 \times \overline{SD}_{\text{diurnal}}$) for summer (**in bold**) is considered the uncertainty associated with GOCI sensor. The root mean squared error (RMSE) from the AERONET-OC data is shown for reference.

	All Seasons			Summer			AERONET-OC
Product	$\pm 2 \cdot \overline{SD}_{diurnal}$ *	$Med[CV[\%]_{diurnal}]$ **	N	$\pm 2 \cdot \overline{SD}_{diurnal}$ *	$Med[CV[\%]_{diurnal}]$ **	N	RMSE*
$R_{rs}(412)$	1.08×10^{-3}	3.90	1160	$\mathbf{8.05 \times 10^{-4}}$	2.60	403	2.2×10^{-3}
$R_{rs}(443)$	7.10×10^{-4}	3.32	1160	$\mathbf{5.49 \times 10^{-4}}$	2.32	403	1.8×10^{-3}
$R_{rs}(490)$	5.40×10^{-4}	3.85	1160	$\mathbf{4.48 \times 10^{-4}}$	2.98	403	2.1×10^{-3}
$R_{rs}(555)$	2.77×10^{-4}	7.57	1160	$\mathbf{2.51 \times 10^{-4}}$	6.72	403	2.3×10^{-3}
$R_{rs}(660)$	9.68×10^{-5}	20.19	1159	$\mathbf{8.83 \times 10^{-5}}$	16.85	403	5.0×10^{-4}
$R_{rs}(680)$	1.08×10^{-4}	17.63	1159	$\mathbf{1.36 \times 10^{-4}}$	20.40	403	N/A
Chl-*a*	1.57×10^{-2}	6.15	1155	$\mathbf{1.09 \times 10^{-2}}$	5.71	401	N/A
$a_g(412)$	2.26×10^{-3}	4.52	1159	$\mathbf{2.09 \times 10^{-3}}$	5.12	402	N/A
POC	4.03	4.91	1159	**3.70**	5.37	402	N/A

* R_{rs} in $[sr^{-1}]$, $Chl-a$ in $[mg\ m^{-3}]$, $a_g(412)$ in $[m^{-1}]$, and POC in $[mg\ m^{-3}]$.
** in [%].

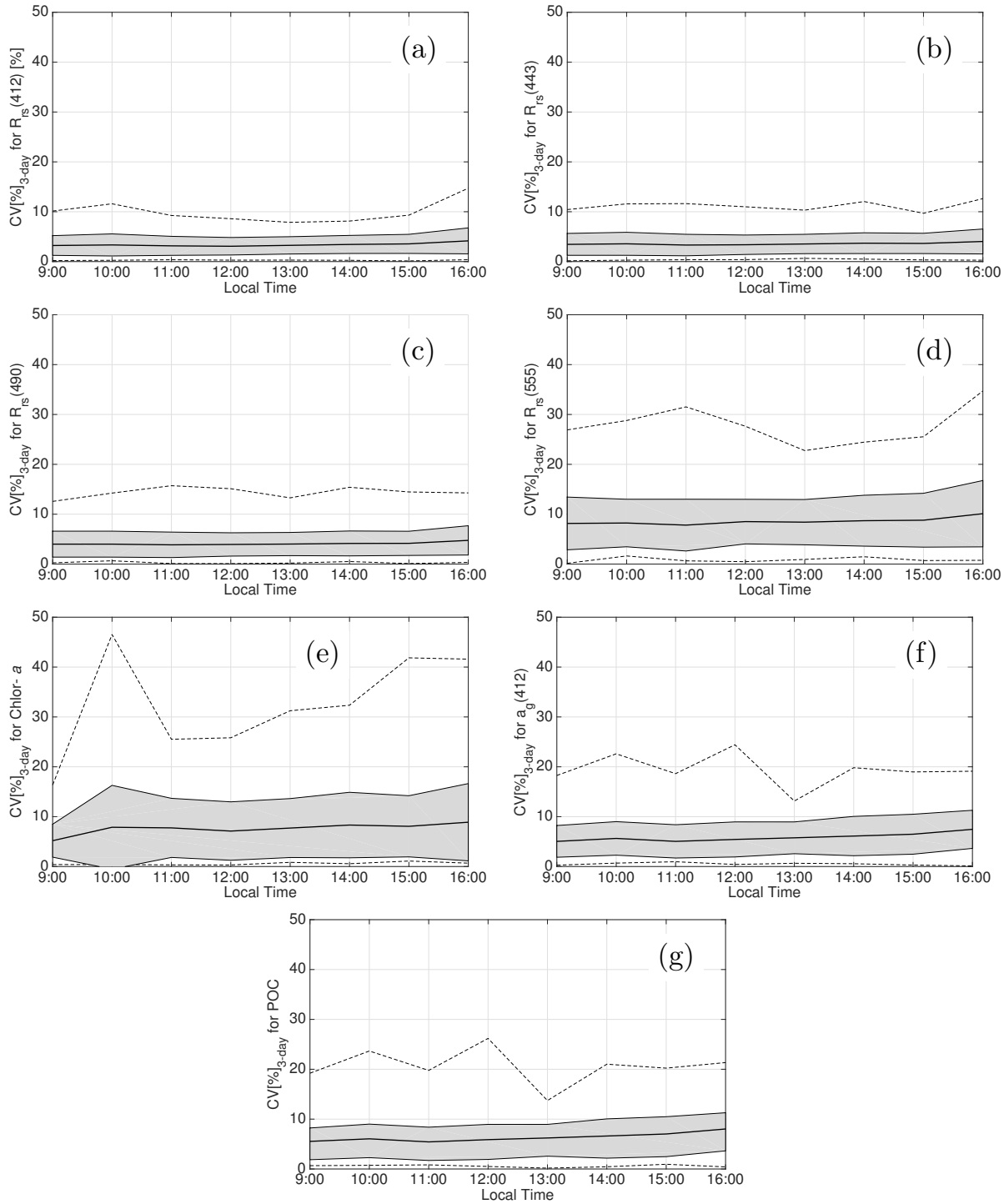

Figure 6. Diurnal variability in R_{rs} and biogeochemical derived products in terms of $CV[\%]_{3\text{-day}}$ for the 96 three-day diurnal sequences of the GOCI-derived products. Minimum (upper dashed line), maximum (lower dashed line), mean (solid black line) and standard deviation (SD) (shaded area).

4.3. Diurnal Differences

In order to obtain a different estimation of the uncertainties over a day, the relative difference of the time of the day, t, with respect to the value at 13:00 hrs ($R\Delta_t[\%]$) was calculated (Table 2; Figure 7). The value at 13:00 hrs was chosen as a reference because it reflects the value that NASA heritage sensors (SeaWiFS, MODIS-Aqua, VIIRS) would measure with similar acquisition time and solar geometry and also because this is the value that should be affected the least by solar geometry (lower solar zenith angle). Assuming temporal homogeneity, we would expect minimal deviation from the value at 13:00 hrs.

If we define the difference with respect to a reference as $\Delta_t = x_t - x_{\text{reference}}$, then, the relative difference for time t is defined as

$$R\Delta_t[\%] = \frac{\Delta_t}{|x_{\text{reference}}|} \times 100[\%] = \frac{x_t - x_{\text{reference}}}{|x_{\text{reference}}|} \times 100[\%] \quad (7)$$

where x_t is the satellite data at the local time t = 09:00, 10:00, ..., 16:00 hrs, and in this case, the reference is the value at 13:00 hrs, i.e. $x_{\text{reference}} = X_{13:00}$. In order to exclude outliers, only relative differences that were within the mean plus 3 times the standard deviation ($mean \pm 3 \times SD$) were included in the analysis. The $R\Delta_t[\%]$ is an indicator of uncertainties that are expected depending on the time of the day, assuming no changes in the water properties due to biological or biogeochemical processes. This analysis was performed for all seasons (all data) and for only summer. Overall, most of the mean $R\Delta_t[\%]$ are below 10% for all bands except the last two hours for the 660 nm band and for most of the times for the 680 nm band (Table 2). The mean $R\Delta_t[\%]$ are smaller or close to 5% for the 412, 443, 490 and 555 nm bands for all times of the day when all the seasons or only summer are considered. For the 660 nm band, the mean $R\Delta_t[\%]$ values for the last two times of day are about 20%. For the 680 nm band, the mean $R\Delta_t[\%]$ values are larger than 10% for all times of the day except the values at 11:00, 12:00 and 14:00 hrs, being significantly large for the last time of day (16:00 hrs). For the blue bands (412, 443, 490 nm), the mean $R\Delta_t[\%]$ is smaller for summer than for all seasons, and generally holds for $R_{\text{rs}}(555)$. The standard deviation of $R\Delta_t[\%]$ is smaller for only summer than all season for most cases. Also, the mean $R\Delta_t[\%]$ for Chl-*a*, POC and $a_g(412)$ for all times of the day are less than 6% (Table 2; Figure 7).

4.4. Products versus solar zenith angle

The variability in R_{rs} and the Chlor-*a*, $a_g(412)$, and POC products versus SZA by season and time of day was investigated to assess the extent to which imperfect atmospheric correction models due to elevated SZA factors, such as higher air mass fraction and lower signal, affect the uncertainty in diurnal product retrievals. GOCI data from the summer period show the lowest level of variability for all hourly observations (Figure 8). Overall, R_{rs} and other products do not seem to be drastically affected negatively by SZA, and no negative or invalid values are recorded at extreme SZA (SZA$> 75^o$). This is an indication that the atmospheric correction model seems to adequately account for solar geometry effects, even at extreme SZA.

Summer is fairly uniform with very narrow variability for all products, meaning the water is fairly stable in the summer regardless of the SZA because the optical properties are not changing. There is a wider range of values for the other seasons, especially in spring due to the higher productivity yielding a wide amplitude in R_{rs} and biogeochemical products (Figure 8). The largest number of valid values is from summer, followed by fall, then spring, being the smallest in winter. In spring and fall, there are almost twice as many valid values than for winter, and three times for summer. For winter, there are more limited observations due to the quality screening criteria excluding data as well as a wider range of values at higher SZA. Similarly to R_{rs}, the derived biogeochemical products demonstrated a wide range of values during spring and narrower distribution during summer.

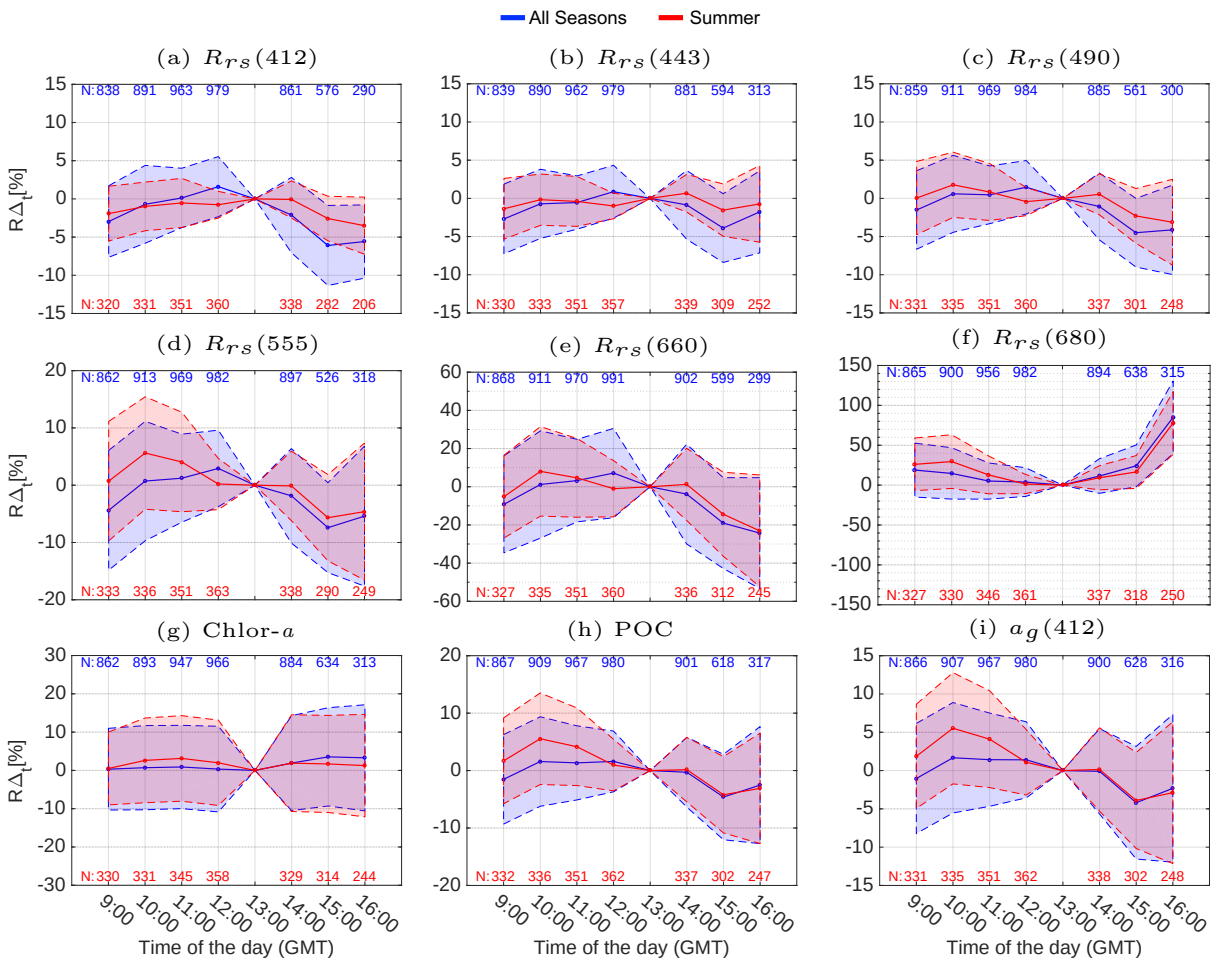

Figure 7. Mean of the relative difference $R\Delta_t[\%]$ with respect to the value at 13:00 hrs for $R_{\mathrm{rs}}(\lambda)$ and (g) Chl-*a*, (h) POC and (i) $a_{\mathrm{g}}(412)$ for all data (blue) and for only Summer (red). The value at 13:00 hrs was selected as a reference because it resembles the NASA heritage sensor acquisition time and solar geometry. Error bars represent one standard deviation (SD). The number of observations used for the statistics annotated above the error bars.

Preprints (www.preprints.org) | NOT PEER-REVIEWED | Posted: 2 November 2018 doi:10.20944/preprints201811.0042.v1

Peer-reviewed version available at Remote Sens. 2019, 11, 295; doi:10.3390/rs11030295

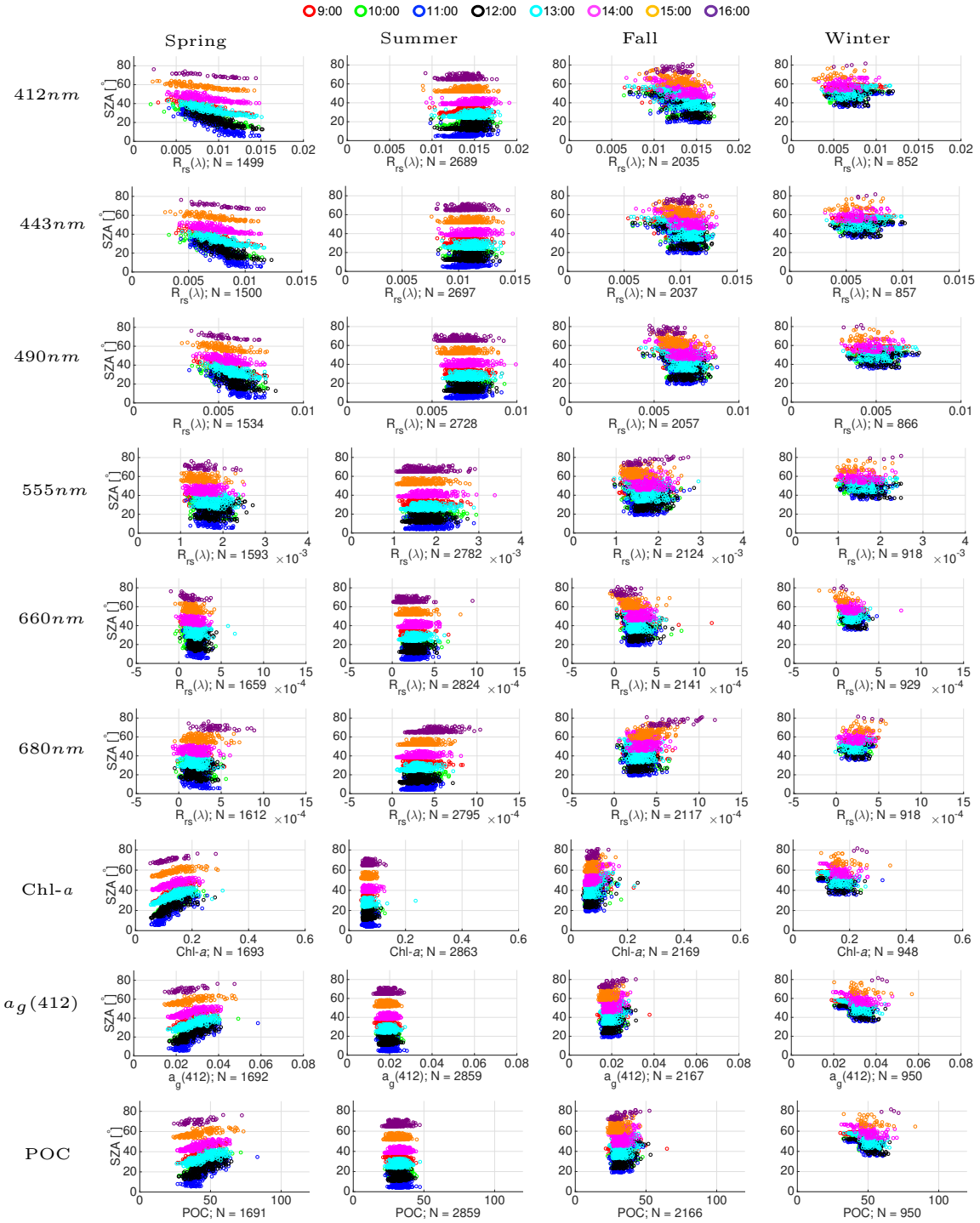

Figure 8. Filtered mean for $R_{\mathrm{rs}}(\lambda)$ and biogeochemical products versus solar zenith angle (SZA) for the GOCI mission from May 2011 to January 2018. Only data that passed the exclusion criteria were used. All SZA values ($(0^o < SZA < 90^o)$) were used. The data are separated by season, and color coded by time of the day.

Table 2. The diurnal variability was also assessed with the relative difference $R\Delta_t[\%]$ with respect to the value at 13:00 hrs. The analysis was performed for all the seasons and for only summer, when there is the smallest variability in the water properties. The mean of the value at 13:00 hrs ($\overline{X}_{13:00}$) is shown for reference.

		$R\Delta_t$[%]: Mean(±SD)							
		Time of the day (Local Time)							
		9:00	10:00	11:00	12:00	13:00	14:00	15:00	16:00
Product*	$\overline{X}_{13:00}$	All Seasons							
$R_{rs}(412)$	1.21×10^{-2}	-2.96 (4.68)	-0.71 (5.10)	0.12 (3.89)	1.60 (3.94)	0.00 (0.00)	-2.12 (4.92)	-6.10 (5.24)	-5.58 (4.80)
$R_{rs}(443)$	9.48×10^{-3}	-2.70 (4.56)	-0.71 (4.53)	-0.55 (3.49)	0.87 (3.45)	0.00 (0.00)	-0.85 (4.50)	-3.89 (4.50)	-1.77 (5.37)
$R_{rs}(490)$	6.39×10^{-3}	-1.52 (5.14)	0.59 (5.04)	0.46 (3.78)	1.46 (3.50)	0.00 (0.00)	-1.06 (4.38)	-4.50 (4.49)	-4.12 (5.85)
$R_{rs}(555)$	1.71×10^{-3}	-4.38 (10.45)	0.73 (10.42)	1.22 (7.69)	2.93 (6.68)	0.00 (0.00)	-1.85 (8.25)	-7.41 (7.85)	-5.40 (12.21)
$R_{rs}(660)$	2.36×10^{-4}	-9.22 (25.40)	1.18 (28.10)	3.22 (21.60)	7.16 (23.38)	0.00 (0.00)	-3.84 (26.11)	-19.01 (23.76)	-24.29 (29.04)
$R_{rs}(680)$	2.64×10^{-4}	18.87 (33.82)	14.65 (32.16)	5.13 (22.67)	3.80 (17.99)	0.00 (0.00)	11.37 (21.67)	24.20 (26.16)	85.11(45.46)
Chl-a	9.40×10^{-2}	0.32 (10.67)	0.71 (10.99)	0.89 (10.88)	0.34 (11.19)	0.00 (0.00)	1.91 (12.39)	3.54 (12.83)	3.28 (13.86)
$a_g(412)$	2.27×10^{-2}	-1.03 (7.19)	1.67 (7.21)	1.42 (6.09)	1.41 (4.97)	0.00 (0.00)	-0.10 (5.57)	-4.20 (7.36)	-2.32 (9.64)
POC	37.30	-1.53 (7.79)	1.57 (7.79)	1.34 (6.45)	1.59 (5.29)	0.00 (0.00)	-0.29 (6.08)	-4.60 (7.44)	-2.53 (10.19)
		Summer							
$R_{rs}(412)$	1.44×10^{-2}	-1.93 (3.58)	-0.98 (3.19)	-0.53 (3.21)	-0.76 (1.75)	0.00 (0.00)	-0.07 (2.42)	-2.57 (2.92)	-3.51 (3.74)
$R_{rs}(443)$	1.09×10^{-2}	-1.37 (3.98)	-0.17 (3.36)	-0.40 (3.26)	-1.00 (1.67)	0.00 (0.00)	0.68 (2.46)	-1.54 (3.43)	-0.72 (5.02)
$R_{rs}(490)$	6.94×10^{-3}	0.04 (4.80)	1.78 (4.27)	0.83 (3.73)	-0.43 (1.83)	0.00 (0.00)	0.53 (2.69)	-2.30 (3.59)	-3.12 (5.61)
$R_{rs}(555)$	1.74×10^{-3}	0.71 (10.43)	5.62 (9.82)	4.06 (8.69)	0.21 (4.47)	0.00 (0.00)	-0.13 (6.07)	-5.67 (7.54)	-4.61 (11.96)
$R_{rs}(660)$	2.55×10^{-4}	-5.20 (21.66)	8.06 (23.45)	4.66 (20.62)	-1.02 (14.72)	0.00 (0.00)	1.24 (18.89)	-14.38 (21.99)	-23.10 (29.26)
$R_{rs}(680)$	2.94×10^{-4}	26.06 (33.02)	29.49 (33.63)	12.81 (23.72)	1.34 (12.06)	0.00 (0.00)	9.21 (15.12)	16.49 (20.60)	77.93 (39.36)
Chl-a	6.51×10^{-2}	0.50 (9.51)	2.62 (11.06)	3.13 (11.17)	1.99 (11.14)	0.00 (0.00)	1.89 (12.63)	1.68 (12.68)	1.26 (13.39)
$a_g(412)$	1.88×10^{-2}	1.86 (6.80)	5.53 (7.27)	4.10 (6.32)	1.08 (4.27)	0.00 (0.00)	0.14 (5.44)	-3.90 (6.27)	-2.88 (9.25)
POC	31.70	1.70 (7.47)	5.54 (7.97)	4.15 (6.76)	0.96 (4.49)	0.00 (0.00)	0.16 (5.62)	-4.21 (6.65)	-3.10 (9.62)

* R_{rs} in $[sr^{-1}]$, $Chl-a$ in $[mgm^{-3}]$, $a_g(412)$ in $[m^{-1}]$, and POC in $[mgm^{-3}]$.

5. Summary and Conclusions

This present study provides an estimation of the uncertainties associated with the study of diurnal variability using the GOCI instrument over a homogeneous study region. The sources of these uncertainties could be from the instrument (e.g. radiometric noise), from the solar and viewing geometry (e.g. SZA), or from processing and algorithms.

R_{rs} and biogeochemical products (Chl-a, CDOM absorption at 412 nm, and particulate organic carbon) were analyzed for nearly the entire GOCI time series (May 2011 to January 2018). An expected seasonal cycle was observed through the whole mission for all products (Figure 3; Figure 4). No negative values were obtained for the R_{rs}, which demonstrates that the atmospheric correction and vicarious calibration are working properly. This was not the case when the data were analyzed using the previous vicarious gains included in SeaDAS. The updated vicarious gains for GOCI by [13] improved the results dramatically.

The temporal and spatial homogeneity of the study area was demonstrated through different analyses. This was a first critical step for posteriorly assessing the uncertainties. First, three-day sequences were used to quantify day-to-day and diurnal variability. This analysis was performed by time of day. Even though an expected significant seasonal pattern can be seenis observed when all the data for the region are shown, this analysis demonstrated that the diurnal and day-to-day variability on of the products is much lower or very minimal compared to the overall mission whenfor the 96 three-day sequences are studied compared to the overall mission. It was shown that GOCI R_{rs} and derived products are similar from the first day to the third day (day-to-day) for each time of day for all bands with a mean of the percent coefficient of variation for the three-day sequences ($CV[\%]_{\text{3-day}}$) smaller than 10% for all products and bands and for all times of day (Figure 5 and Figure 6). Second, diurnal statistics were used to test homogeneity. The $Med[CV[\%]_{\text{diurnal}}]$ are small ($< 7\%$) for all products except the red bands, indicating a small variability occurring over the day, and therefore demonstrating homogeneity (Table 1). These results demonstrate that the region of study is very homogenous. They also help to understand the base level of uncertainties over the course of a day,

and therefore, that a larger value could be considered a change in water properties associated with biological, biogeochemical or physical processes.

We consider that an approximate measure of the threshold or minimum difference required for R_{rs} (or derived products) to detect diurnal, or day-to-day change in GOCI is considered to be two times the mean diurnal SD values (i.e. $2 \times \overline{SD}_{diurnal}$) for summer for the GCWS region (Table 1). This estimation of variability was determined from summer because in this season there is less variability due to change in the water properties (Figure 8). The $2 \times \overline{SD}_{diurnal}$ for the R_{rs} retrievals at 412, 443, 490, 555, 660 and 680 are 8.05×10^{-4}, 5.49×10^{-4}, 4.48×10^{-4}, 2.51×10^{-4}, 8.83×10^{-5}, and 1.36×10^{-4} sr^{-1}, respectively, and 1.09×10^{-2} mg m^{-3} for Chl-*a*, 2.09×10^{-3} m^{-1} for $a_g(412)$, and 3.7 mg m^{-3} for POC. The $2 \times \overline{SD}_{diurnal}$ values are at least three times smaller for all bands (412-660 nm) when compared with the RMSE from the matchups from AERONET-OC data. The RMSE values from AERONET-OC are an estimation of the uncertainties for more productive waters and under more challenging atmospheric conditions, while $2 \times \overline{SD}_{diurnal}$ provide uncertainties levels under more constant oceanic atmospheric conditions. Therefore, the changes in water properties retrieved by GOCI should at least be greater than $2 \times \overline{SD}_{diurnal}$ to be considered a change in water properties due to biological, physical or biogeochemical processes.

Overall, the relative difference with respect to the value at 13:00 hrs ($R\Delta t[\%]$) are less than 10% for all products except the $R_{rs}(680)$, and there is no indication of skewing of the diurnal variability due to processing (Table 2; Figure 7). A similar behavior occurs for the other biogeochemical products examined, with a relative difference less than 5% for all times of the day. The behavior of the different products with respect to the SZA was analyzed in order to determine any trend caused by the atmospheric correction and SZA (Figure 8). When the GOCI data versus SZA were analyzed, separated by seasons and by time of day, no trend was observed. Summer seems to yield the best data to work with for evaluating GOCI in this study area because of the very narrow variability for all products. Spring is more variable in the Chl-a levels, as a consequence of phytoplankton production (Figure 8). The same behavior can be seen for $a_g(412)$ and POC. From these two analyses, it seems that the time of day, and therefore the SZA, does not have a significant negative impact on the results that passed the filtering criteria, demonstrating that the atmospheric correction algorithm is working adequately, even at extreme SZA (SZA$> 75^o$). It is worth pointing out that this holds true only if a proper vicarious calibration is applied. Before updating the vicarious gains, low or negative R_{rs} values were observed at extreme SZA.

We acknowledge the fact that some diurnal variability occurs in the GCWS due to biogeochemical or biological processes, and these changes are not included in our analysis. However, we believe that this variability is minimal, especially in summer, and the GCWS is homogeneous in time and space with no diurnal trend.

As a general conclusion, the diurnal variability estimates determined in this study provide a guide as to the minimum value of diurnal change that must be observed to overcome uncertainties in instrument radiometric noise and algorithm processing. Our future work will apply these results to estimate changes in diurnal and day-to-day biogeochemical stocks and processes in coastal oceans using GOCI.

Author Contributions: conceptualization, J.C. and A.M.; methodology, J.C. and A.M.; software, J.C.; validation, J.C.; formal analysis, J.C.; investigation, J.C.; resources, J.C.; data curation, J.C.; writing—original draft preparation, J.C and A.M.; writing—review and editing, J.C, A.M., B.F. and W.K.; visualization, J.C.; supervision, A.M and B.F.; project administration, A.M. and B.F.; funding acquisition, A.M. and B.F.

Funding: This research was funded by NASA Earth Science U.S. Participating Investigator (NNH12ZDA001N-ESUSPI).

Acknowledgments: We thank the Korea Ocean Satellite Center for providing the GOCI L1B data.

Conflicts of Interest: The authors declare no conflict of interest.

References

1. Esaias, W.; Abbott, M.; Barton, I.; Brown, O.B.; Campbell, J.; Carder, K.; Clark, D.; Evans, R.; Hoge, F.E.; Gordon, H.; Balch, W.; Letelier, R.; Minnett, P. An overview of MODIS capabilities for ocean science observations. *Geoscience and Remote Sensing, IEEE Transactions on* **1998**, *36*, 1250–1265. doi:10.1109/36.701076.
2. Goldberg, M.D.; Kilcoyne, H.; Cikanek, H.; Mehta, A. Joint Polar Satellite System: The United States next generation civilian polar-orbiting environmental satellite system. *Journal of Geophysical Research: Atmospheres*, *118*, 13,463–13,475, [https://agupubs.onlinelibrary.wiley.com/doi/pdf/10.1002/2013JD020389]. doi:10.1002/2013JD020389.
3. Ryu, J.H.; Han, H.J.; Cho, S.; Park, Y.J.; Ahn, Y.H. Overview of geostationary ocean color imager (GOCI) and GOCI data processing system (GDPS). *Ocean Science Journal* **2012**, *47*, 223–233. doi:10.1007/s12601-012-0024-4.
4. Ryu, J.H.; Choi, J.K.; Ahn, J.H. Temporal variation in Korean coastal waters using Geostationary Ocean Color Imager. Special Issue 64, 2011, pp. 1731–1735. ISSN 0749-0208.
5. Kim, W.; Moon, J.E.; Park, Y.J.; Ishizaka, J. Evaluation of chlorophyll retrievals from Geostationary Ocean Color Imager (GOCI) for the North-East Asian region. *Remote Sensing of Environment* **2016**, *184*, 482 – 495. doi:https://doi.org/10.1016/j.rse.2016.07.031.
6. He, X.; Bai, Y.; Pan, D.; Huang, N.; Dong, X.; Chen, J.; Chen, C.T.A.; Cui, Q. Using geostationary satellite ocean color data to map the diurnal dynamics of suspended particulate matter in coastal waters. *Remote Sensing of Environment* **2013**, *133*, 225 – 239. doi:http://dx.doi.org/10.1016/j.rse.2013.01.023.
7. Hu, Z.; Pan, D.; He, X.; Bai, Y. Diurnal Variability of Turbidity Fronts Observed by Geostationary Satellite Ocean Color Remote Sensing. *Remote Sensing* **2016**, *8*, 147. doi:10.3390/rs8020147.
8. Kim, H.; Son, Y.B.; Jo, Y.H. Hourly Observed Internal Waves by Geostationary Ocean Color Imagery in the East/Japan Sea. *Journal of Atmospheric and Oceanic Technology* **2018**, *35*, 609–617, [https://doi.org/10.1175/JTECH-D-17-0049.1]. doi:10.1175/JTECH-D-17-0049.1.
9. Noh, J.H.; Kim, W.; Son, S.H.; Ahn, J.H.; Park, Y.J. Remote quantification of Cochlodinium polykrikoides blooms occurring in the East Sea using geostationary ocean color imager (GOCI). *Harmful Algae* **2018**, *73*, 129 – 137. doi:https://doi.org/10.1016/j.hal.2018.02.006.
10. Son, Y.B.; Choi, B.J.; Kim, Y.H.; Park, Y.G. Tracing floating green algae blooms in the Yellow Sea and the East China Sea using GOCI satellite data and Lagrangian transport simulations. *Remote Sensing of Environment* **2015**, *156*, 21 – 33. doi:https://doi.org/10.1016/j.rse.2014.09.024.
11. Ruddick, K.; Neukermans, G.; Vanhellemont, Q.; Jolivet, D. Challenges and opportunities for geostationary ocean colour remote sensing of regional seas: A review of recent results. *Remote Sensing of Environment* **2014**, *146*, 63 – 76. Liege Colloquium Special Issue: Remote sensing of ocean colour, temperature and salinity, doi:http://dx.doi.org/10.1016/j.rse.2013.07.039.
12. Kang, G.; Coste, P.; Youn, H.; Faure, F.; Choi, S. An In-Orbit Radiometric Calibration Method of the Geostationary Ocean Color Imager. *IEEE Transactions on Geoscience and Remote Sensing* **2010**, *48*, 4322–4328. doi:10.1109/TGRS.2010.2050329.
13. Concha, J.; Mannino, A.; Franz, B.A.; Bailey, S.; Kim, W. GOCI's Vicarious Calibration for the SeaDAS/l2gen package. *International Journal of Remote Sensing* **2018**.
14. Kim, W.; Ahn, J.H.; Park, Y.J. Correction of Stray-Light-Driven Interslot Radiometric Discrepancy (ISRD) Present in Radiometric Products of Geostationary Ocean Color Imager (GOCI). *IEEE Transactions on Geoscience and Remote Sensing* **2015**, *53*, 5458–5472. doi:10.1109/TGRS.2015.2422831.
15. Kim, W.; Moon, J.E.; Ahn, J.H.; Park, Y.J. Evaluation of Stray Light Correction for GOCI Remote Sensing Reflectance Using in Situ Measurements. *Remote Sensing* **2016**, *8*. doi:10.3390/rs8050378.
16. Qiu, B. Kuroshio And Oyashio Currents. In *Encyclopedia of Ocean Sciences*; Steele, J.H., Ed.; Academic Press: Oxford, 2001; pp. 1413 – 1425. doi:https://doi.org/10.1006/rwos.2001.0350.
17. McClain, C.R.; Signorini, S.R.; Christian, J.R. Subtropical gyre variability observed by ocean-color satellites. *Deep Sea Research Part II: Topical Studies in Oceanography* **2004**, *51*, 281 – 301. Views of Ocean Processes from the Sea-viewing Wide Field-of-view Sensor (SeaWiFS) Mission: Volume 1, doi:https://doi.org/10.1016/j.dsr2.2003.08.002.

18. Signorini, S.R.; Franz, B.A.; McClain, C.R. Chlorophyll variability in the oligotrophic gyres: mechanisms, seasonality and trends. *Frontiers in Marine Science* **2015**, *2*, 1. doi:10.3389/fmars.2015.00001.
19. Bailey, S.W.; Werdell, P.J. A multi-sensor approach for the on-orbit validation of ocean color satellite data products. *Remote Sensing of Environment* **2006**, *102*, 12 – 23. doi:http://dx.doi.org/10.1016/j.rse.2006.01.015.
20. Gordon, H.R.; Wang, M. Retrieval of water-leaving radiance and aerosol optical thickness over the oceans with SeaWiFS: a preliminary algorithm. *Appl. Opt.* **1994**, *33*, 443–452.
21. Bailey, S.W.; Franz, B.A.; Werdell, P.J. Estimation of near-infrared water-leaving reflectance for satellite ocean color data processing. *Opt. Express* **2010**, *18*, 7521–7527. doi:10.1364/OE.18.007521.
22. Ahmad, Z.; Franz, B.A.; McClain, C.R.; Kwiatkowska, E.J.; Werdell, J.; Shettle, E.P.; Holben, B.N. New aerosol models for the retrieval of aerosol optical thickness and normalized water-leaving radiances from the SeaWiFS and MODIS sensors over coastal regions and open oceans. *Appl. Opt.* **2010**, *49*, 5545–5560. doi:10.1364/AO.49.005545.
23. O'Reilly, J.; Maritorena, S.; Mitchell, B.; Siegel, D.; Carder, K.; Garver, S.; Kahru, M.; McClain, C. Ocean color chlorophyll algorithms for SeaWiFS. *JOURNAL OF GEOPHYSICAL RESEARCH-OCEANS* **1998**, *103*, 24937–24953. doi:{10.1029/98JC02160}.
24. Hu, C.; Lee, Z.; Franz, B. Chlorophyll-a algorithms for oligotrophic oceans: A novel approach based on three-band reflectance difference. *Journal of Geophysical Research* **2012**, *Volume 117, Issue C1*.
25. Stramski, D.; Reynolds, R.A.; Babin, M.; Kaczmarek, S.; Lewis, M.R.; Röttgers, R.; Sciandra, A.; Stramska, M.; Twardowski, M.S.; Franz, B.A.; Claustre, H. Relationships between the surface concentration of particulate organic carbon and optical properties in the eastern South Pacific and eastern Atlantic Oceans. *Biogeosciences* **2008**, *5*, 171–201. doi:10.5194/bg-5-171-2008.
26. Mannino, A.; Novak, M.G.; Hooker, S.B.; Hyde, K.; Aurin, D. Algorithm development and validation of {CDOM} properties for estuarine and continental shelf waters along the northeastern U.S. coast. *Remote Sensing of Environment* **2014**, *152*, 576 – 602. doi:https://doi.org/10.1016/j.rse.2014.06.027.
27. Mobley, C.; Werdell, P.; Franz, B.; Ahmad, Z.; Bailey, S. Atmospheric Correction for Satellite Ocean Color Radiometry. Technical Report NASA/TM-2016-217551, NASA Goddard Space Flight Center, 2016.